# Optimization of the thermal field of 8-inch SiC crystal growth by PVT method with "3 separation heater method"

Binjie Xu [a,b], Xuefeng Han [a,b,*], Suocheng Xu [c], Deren Yang [a,b], Xiaodong Pi [a,b,*]

[a] State Key Laboratory of Silicon Materials & School of Materials Science and Engineering, Zhejiang University, Hangzhou 310027, China
[b] Zhejiang Provincial Key Laboratory of Power Semiconductor Materials and Devices, ZJU-Hangzhou Global Scientific and Technological Innovation Center, Hangzhou 311200, China
[c] IV Semitec Co., Ltd., Hangzhou 311200, China

## ARTICLE INFO

## ABSTRACT

Silicon carbide (SiC) has important application prospects in power and radio frequency (RF) devices. However, preparing large-diameter, high-quality SiC crystals is challenging. The major technique for growing large-diameter SiC crystals is the physical vapor transport (PVT) method and the key point for adjusting conditions is to find an optimal thermal field. In this study, we propose a resistance heating method called the "3 separation heater method" with 3 heaters separated by the graphite foam insulations so that 3 important parts (the SiC source powder area, SiC seed area, and seed holder) of the growth cell can be heated independently through thermal radiation from each separated heater. Further, the insulation separators play an important role as a switch of the heat flux. The numerical studies of the thermal field design for this model are conducted with the help of the numerical simulation software COMSOL Multiphysics and its appropriate parameters are explored. At last, the relationship between the parameters and crystal growth conditions, such as the radial temperature difference (RTD) and edge temperature gradient (ETG), is expressed by the back-propagation (BP) neural network and the optimal parameter values for crystal growth conditions have been confirmed using the non-dominated sorting genetic algorithm (NSGA-II).

## 1. Introduction

Due to the advantages of the wide band gap, high breakdown field strength, high thermal conductivity, and high carrier mobility [1–4], silicon carbide (SiC), particularly 4H-SiC, has received widespread attention in the application of high-power and high-frequency electronics, such as electrical vehicles, 5G communications, and renewable-energy systems [5,6]. Low-defect-density, low-cost, and large-size are fundamental for the fabrication of SiC devices.

The major technique for growing large-size SiC crystals is the physical vapor transport (PVT) method, which evolves from the Lely method developed in 1955 by Lely J.A through a sublimation process [7]. However, the Lely method cannot effectively control the growth of the single crystal. Tairov and Tsvetkov pioneered the seeded sublimation method to grow SiC single crystal in 1977, which is also called the "modified Lely method", or PVT method [8,9]. Remarkable improvement in SiC growth technology has been made in recent decades, Ziegler et al. and Augustine et al. [10] successively improved the method proposed by Tairov and Tsvetkov, to successfully grow large-size and high-quality SiC crystals.

In this method, SiC powder is used as the source material placed at the bottom of a cylindrical dense graphite crucible, a SiC seed crystal is placed near the lid of the crucible, and a high-purity Ar (or He) flow is employed for growth [11]. In the crystal growth process, the SiC powder is sublimated by the high temperature into gas-phase species consisting of Si, $Si_2C$, and $SiC_2$ [12]. Then they will be transported to the surface of the seed crystal through a process of convection and diffusion, in which the 3 species will also be transformed into each other through chemical reactions [13]. At last, they deposit and crystallize on the seed crystal because the vapor is supersaturated near the seed for the relatively lower temperature [14]. Adjusting conditions to find an optimal thermal field is a key point to improve the crystal quality since the temperature difference is a driving force for gas phase species transport and deposition on crystal seed [15–17].

The application of the SiC device is limited by the high manufacturing cost of SiC substrates, therefore, 8-inch SiC will become the mainstream in industrial production due to its low cost-yield ratio and large-size advantage [18]. However, with the diameter increase from

150 mm to 200 mm, the difficulty of multiple physical field control multiplies, especially with the thermal field control, which plays a decisive role in the growth of large-size SiC crystals. The crucible becomes larger with the expansion of crystal diameter, which causes an increase of the thermal resistance from outside to inside. As a consequence, the central temperature of the crystal and source powder decreases, and simultaneously the radial temperature difference (RTD) increases, resulting in a greater convexity of the crystal shape, which will induce polytypes [19], cracks, and the increase of micro defects such as micropipes and dislocations [20,21] because higher convexity always implies higher internal stress. Further, the relatively high temperature at the edge of the source powder region causes the decomposition rate to be higher than that in the center, resulting in a strong gas flow near the crucible wall. As well, there are abundant carbon sources on the crucible wall. Consequently, the growth rate of the outer edge of the crystal is enhanced. This phenomenon will lead to an "M" shape crystal, which always evolves with the poly-crystal surrounding it [17]. All in all, during SiC crystal growth, a nearly flat, slightly convex surface with smooth edge morphology gives birth to high-quality crystals. Therefore, we need to find an optimal thermal field with a low RTD on the surface of the seed crystal to avoid large convexity, and with a large edge temperature gradient (ETG) to counteract the influence of the strong gas flow and abundant carbon sources at the edge to avoid the "M" shape crystals.

From an experimental point of view, the PVT method is a semi-closed black box growth method and we lack the method to measure the crystal growth surface temperature directly [22]. Therefore, numerical studies are carried out to aid experimental studies of PVT nowadays, which can reliably predict experimental results in a short time and greatly reduce experimental costs [14,17,23–30]. With the application of numerical simulation, Nishizawa et al. successfully established stable growth of a constant-diameter SiC ingot by optimizing the shape and location of the "liner" inside the crucible, obtaining high-quality single crystals [31]. Based on the optimized condition by numerical simulation, Zhao et al. obtained a uniformly deposited 8-inch polycrystal with a minimum thickness of 9.6 mm, and the convexity was reduced to 6.4 mm, compared with the original scheme of 13 mm [32]. The simulation provides good guidance in optimizing the crucible geometry and operating parameters. In this study, we propose numerical studies of the thermal field design and optimization for resistance heating 8-inch SiC bulk crystal growth by the finite element method (FEM) analysis in the COMSOL Multiphysics. The resistance heating method of our growth furnace is called the "3 separation heater method", in which 3 heaters are separated by the graphite foam insulations. At last, we have explored the optimal crystal growth condition through the back-propagation (BP) neural network and the non-dominated sorting genetic algorithm (NSGA-II), enabled by the commercial software MATLAB.

## 2. Methods

### 2.1. Numerical model of heat transfer

The FEM enabled by the COMSOL Multiphysics software is employed to investigate the thermal field of SiC crystal growth. Fig. 1(a) shows the 2D axis-symmetric global model for the designed "3 separation heater method" PVT furnace. As is seen, this model consists of graphite foam insulation, resistance heater, graphite crucible, SiC powder, seed crystal, and seed holder, whose feature is that 3 resistance heaters are separated by the graphite foam insulations. Computational grids are constructed, shown in Fig. 1(b), with 12914 mesh cells generated in total.

Unlike the induction heating type, the heat source of the resistance heating type is a resistive heating element, and the power is controlled by changing the current with a consistent voltage. For the growth of SiC crystal by the PVT method, there are 3 important areas in the growth
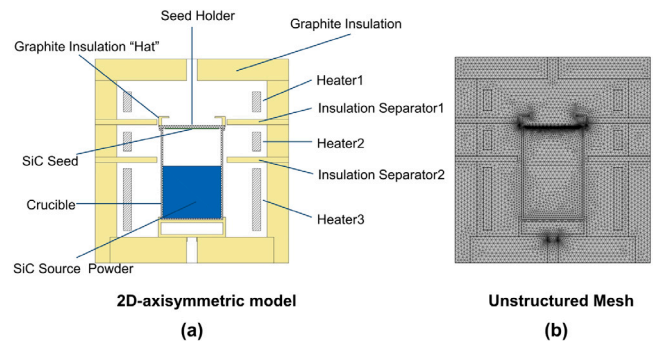


**Fig. 1.** (a) Configuration of the designed "3 separation heater method" PVT furnace; (b) The meshing of the calculation model.
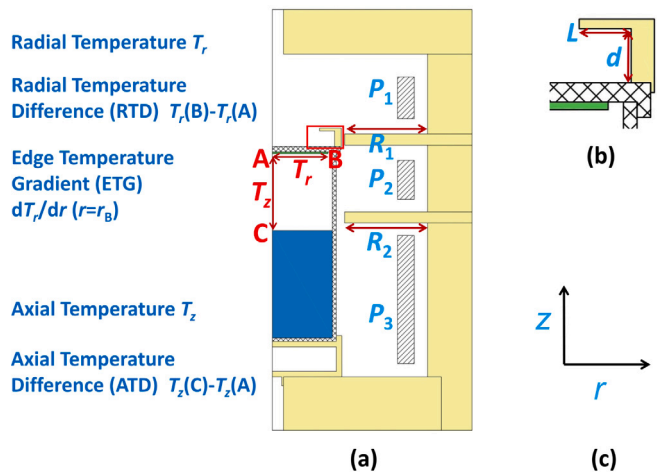


**Fig. 2.** (a) Schematic diagram of each parameter that can be adjusted in this system; (b) The enlargement of the graphite insulation "hat" in red rectangle in (a); (c) The radial (horizontal) axis "*r*" and axial (vertical) axis "*z*".

cell: the SiC source powder area, SiC seed area, and seed holder. The biggest advantage of the method in this study is that the outer wall of these important areas can be heated through thermal radiation from each separated heater respectively, to realize the control of the thermal field in each area.

In this study, the global heat transfer includes radiation heat exchange in gas between solid surfaces, heat conduction in solid media, heat conduction, and convection in the gas, which are taken into consideration to calculate the thermal field. The heat conduction is described by the following stationary equation [29,33]:

$$\nabla \cdot (-k\nabla T) + \rho C_p u \cdot \nabla T - Q = 0, \tag{1}$$

where $Q$ stands for the heater source; $C_p$ for the thermal capacity; $k$ for temperature-dependent thermal conductivity; $\nabla T$ for the temperature gradient; $\rho$ for the material density; $u$ for the fluid flow velocity.

The radiative heat flux at the boundaries is calculated as:

$$q_\sigma = \varepsilon \sigma (T_\infty^4 - T_\sigma^4), \tag{2}$$

where $\varepsilon$ denotes the emissivity; $\sigma$ is the Stephen Boltzmann constant; $T_\infty$ and $T_\sigma$ are the ambient temperature and boundary temperature, respectively.

Further, we have also taken the latent heat during SiC growth into consideration:

$$q_L = \rho v L, \tag{3}$$

where $q_L$ is the released heat per unit area during the crystallization; $\rho$ is the density of SiC crystal with a value of 3160 kg/m³; $v$ is the crystal
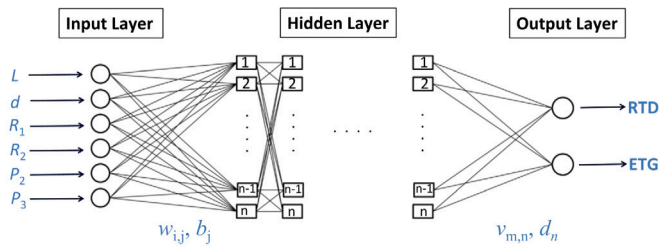
**Fig. 3.** Typical structure of the BP network with 6 inputs, 2 outputs, and hidden layers.
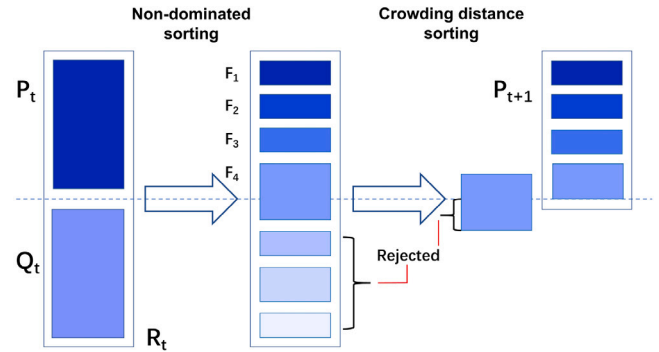


**Fig. 4.** NSGA-II procedure.

growth rate and $L$ is the latent heat of deposition with a value of 5730 kJ/kg [30].

Fig. 2(a) shows the schematic diagram of each parameter that can be adjusted to optimize the thermal field in this system. $R_1$ and $R_2$ stand for the length of the graphite foam insulation separators; $P_1$, $P_2$, and $P_3$ denote the power of each resistance heater. Fig. 2(b) shows the enlargement of the graphite insulation "hat" on the seed holder, which is used to optimize the radial temperature distribution curve on the seed crystal surface. $L$ stands for the length of the "brim" and $d$ for the height. Fig. 2(c) displays the radial (horizontal, indicated by "$r$") and axial (vertical, indicated by "$z$") axis. The RTD of the seed crystal surface is shown as $T_r(B)$ - $T_r(A)$, the axial temperature difference (ATD) from the center of the SiC source powder to the center of the seed crystal is shown as $T_z(C)$ - $T_z(A)$, and the ETG is the slope of the temperature curve at the edge of the seed crystal, denoted by $dT_r/dr(r = r_B)$. The RTD and ETG can effectively control the shape of crystal growth, and the gradient of ATD directly controls the crystal growth rate ($G$), which is calculated as [34]:

$$G = \frac{c \exp(a - b/T_s)(\text{ATD}/L_z)}{T_s^{1.2} P_{argon}}, \tag{4}$$

where $a$, $b$, and $c$ are the constants with values of 30.77, $6.71 \times 10^4$, and $4.22 \times 10^{-6}$, respectively, $T_s$ denotes the temperature on the SiC crystal surface, $P_{argon}$ stands for the Ar pressure, and $L_z$ is the distance between the SiC seed crystal and source powder.

### 2.2. BP neural network and NSGA-II algorithm

When we go further to optimize the thermal field in this design, it is needed to identify the functional relationship between these parameters and the growth conditions first. However, dealing with such a huge amount of data is difficult for COMSOL Multiphysics. Thus, this work can be done by using artificial neural networks (ANN) [35–38]. In this study, we choose the back-propagation (BP) neural network [38–40] to quickly map the complex non-linear relationships between the optimizing parameters ($L$, $d$, $R_1$, $R_2$, $P_2$, and $P_3$) and targets (the RTD and ETG). Then, the non-dominated sorting genetic algorithm

(NSGA-II) is deployed to find the optimal parameters of the thermal field [41–43], and we set the optimal growth condition as the RTD closest to 10 K and ETG as large as possible in this study. Both of the algorithms are realized with the commercial software MATLAB.

Fig. 3 shows the typical structure of a BP neural network, consisting of 3 layers: input, hidden, and output layers. In this study, the 6 inputs are the parameters in our design: $L$, $d$, $R_1$, $R_2$, $P_2$, and $P_3$; the 2 outputs are the RTD and ETG; $w_{ij}(v_{mn})$ represents the weight value of the connection from the $i(m)$th neuron of the proceeding layer to the $j(n)$th neuron of the receiving layer, $b_j$ and $d_n$ are the threshold values of each layer. The numbers of hidden layers and neurons in each hidden layer are uncertain, which determines the accuracy and speed of the predictions of outputs.

The BP neural network consists of the signal propagation and the back-propagation of the error. In the signal propagation process, the input layer receives the inputs, then the inputs are processed, propagated to the next level, and processed, until the outputs layer. For the back-propagation of the error, the errors between the outputs and targets are back-propagated and the weight or threshold values are amended to minimize the errors and accurately reflect the relationship between the inputs and targets. The details and equations of the processes were described in the previous work [44] by Huang et al.

GA is a class of parallel iterative algorithms with certain learning abilities, inspired by the core idea of "survival of the fittest" and "natural selection" from the theory of evolution [45,46]. The sets of variables are coded and considered as "chromosomes" representing individuals, which experience selection, crossover, and mutation after initialization in the evolution process until the stopping condition is satisfied. The details and equations of the processes were described in the previous work [40] by Li et al.

However, for a problem of multi-objective optimization, there is no unique solution that can optimize all the objectives at the same time. That is, there is a conflicted relationship between the objective functions, and the optimal solution is usually a series of solutions. Therefore, the non-dominated sorting genetic algorithm (NSGA-II), whose optimal solution is a set of Pareto front solutions (a solution set that is not dominated by any other solution), is employed to search for the non-dominated solutions. The so-called domination of solutions can be explained that, for a bi-objective optimization problem of minimization, if $f_1(x_1) < f_1(x_2)$ and $f_2(x_1) < f_2(x_2)$ (or $f_1(x_1) > f_1(x_2)$ and $f_2(x_1) > f_2(x_2)$), it is defined that $x_2$ is dominated by $x_1$ (or $x_1$ is dominated by $x_2$), otherwise, $x_1$ and $x_2$ are not dominated by each other. Lastly, we choose one candidate solution that both targets are in good condition as the optimal solution.

NSGA-II introduces a fast non-dominant sorting method, density estimation, crowded comparison operator as well as elitism, and its procedure is shown in Fig. 4 [47,48]. At first, an initial population $P_0$ is created and sorted based on the non-domination. Then, it is used to generate an equal-size population $Q_0$ by the selection, crossover, and mutation operators. Science elitism is introduced by comparing the current population with previously found best non-dominated solutions, the non-dominated sorting algorithm is applied to rank the solutions in a combined population $R_t = P_0 \cup Q_0$, and solutions with smaller front values are remained, just like $F_1$, $F_2$, and $F_3$ in Fig. 4. For the last non-dominated set $F_i$ that the next equal-size population cannot accommodate all the solutions in it, just like $F_4$ in Fig. 4, they are sorted by the crowded-comparison operator in descending order, and the best solutions are chosen to fill all population slots. Fig. 4 shows the $t$th generation of the NSGA-II Algorithm, a new equal-size population $P_{t+1}$ is generated and it will be used for selection, crossover, and mutation to create a new equal-size population $Q_{t+1}$. Such steps are continued until only one frontier is left.
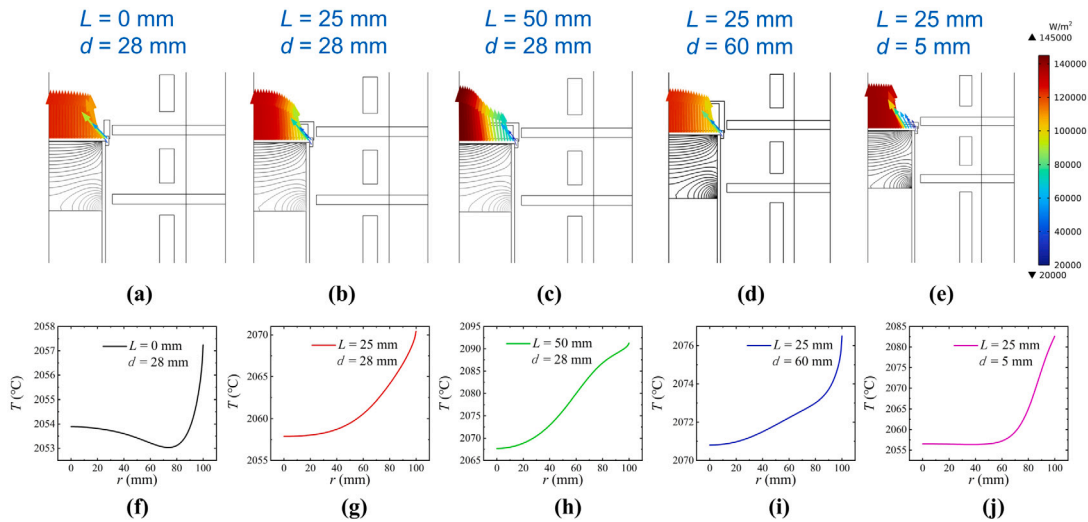
**Fig. 5.** Schematic diagrams of the heat flux (denoted by arrows) and isothermals for (a) $L = 0$ mm, $d = 28$ mm; (b) $L = 25$ mm, $d = 28$ mm; (c) $L = 50$ mm, $d = 28$ mm; (d) $L = 25$ mm, $d = 60$ mm; (e) $L = 25$ mm, $d = 5$ mm. The radial temperature distribution on the seed crystal surface for (f) $L = 0$ mm, $d = 28$ mm; (g) $L = 25$ mm, $d = 28$ mm; (h) $L = 50$ mm, $d = 28$ mm; (i) $L = 25$ mm, $d = 60$ mm; (j) $L = 25$ mm, $d = 5$ mm.
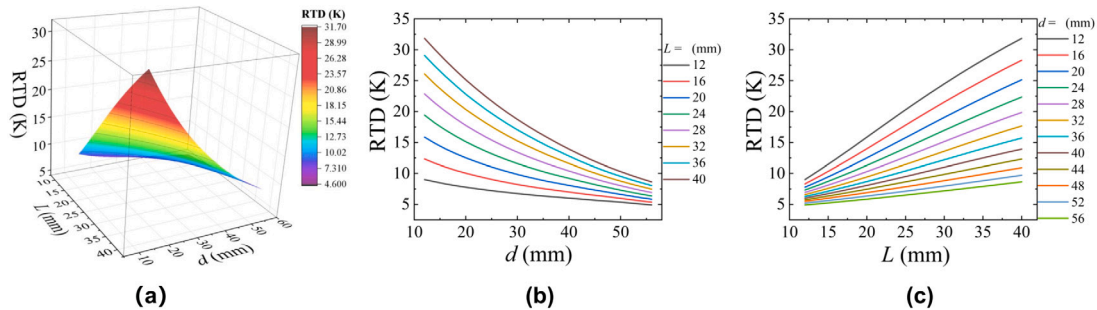


**Fig. 6.** (a) $L$ and $d$ dependence of the RTD, shown as the 3-D view; (b) $d$ dependence of the RTD for different $L$; (c) $L$ dependence of the RTD for different $d$.
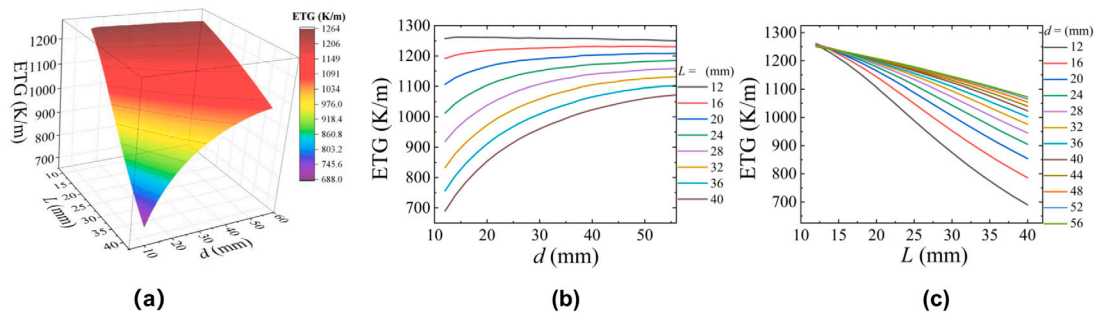


**Fig. 7.** (a) $L$ and $d$ dependence of the ETG, shown as the 3-D view; (b) $d$ dependence of the ETG for different $L$; (c) $L$ dependence of the ETG for different $d$.

## 3. Result and discussion

### 3.1. The role of graphite insulation "hat"

In this design, we set a graphite insulation "hat" to change the path and magnitude of heat flux, which can adjust the radial temperature distribution curve on the seed crystal surface (from point $A$ to point $B$ in Fig. 2), as shown in Fig. 5 with the parameters $R_1 = R_2 = 150$ mm; $P_1 = 1$ kW; $P_2 = 3$ kW and $P_3 = 23$ kW. As $L$ and $d$ vary, the shape of the radial temperature distribution curve changes. As discussed in the Introduction section, the shape of the SiC crystal is determined by the radial temperature curve, which plays a decisive role in crystal quality, the graphite insulation "hat" therefore has a direct influence on the SiC crystal growth.

Fig. 6 shows the $L$ and $d$ dependence of the RTD, it is seen that the RTD decreases with the increase of $d$, to the contrary, it increases as $L$ increases. The reason for this phenomenon has been displayed in Fig. 5, as $L$ increases, the magnitude of the heat released from the part near the edge of the seed holder decreases, and the magnitude released from the area around the center increases, the edge temperature will be relatively high and the RTD will increase as a result. For the increase of $d$, the heat released from the area around the center of the seed holder reduces and that released near the edge enlarges, therefore, the edge temperature will drop relative to the center. With these two factors, it is easy to understand the behavior of the RTD shown in Fig. 6.

Fig. 7 shows the $L$ and $d$ dependence of the ETG, which exhibits the opposite behavior of the RTD. It increases with the increase of $d$ and decreases as $L$ increases, as shown in Fig. 7(b) and (c). This is
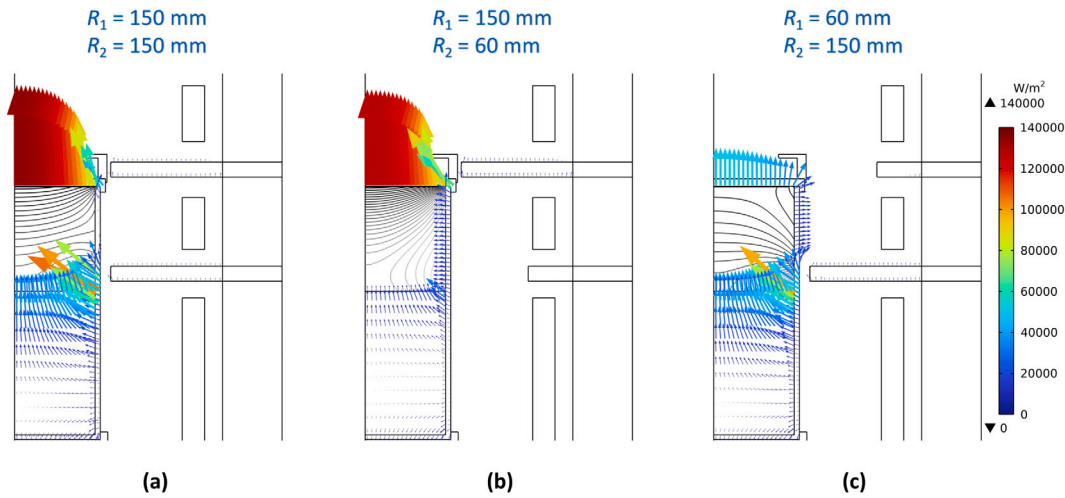
**Fig. 8.** Schematic diagrams of the heat flux (denoted by arrows) and isothermals for (a) $R_1 = 150$ mm, $R_2 = 150$ mm; (b) $R_1 = 60$ mm, $R_2 = 150$ mm; (c) $R_1 = 150$ mm, $R_2 = 60$ mm.
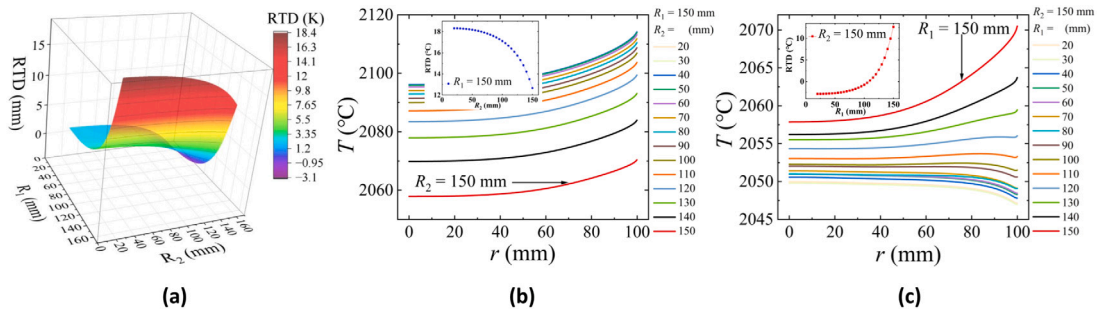


**Fig. 9.** (a) $R_1$ and $R_2$ dependence of the RTD, shown as the 3-D view; the radial temperature distribution with (b) $R_1 = 150$ mm and (c) $R_2 = 150$ mm; and the insets in (b) and (c) show the $R_2$ and $R_1$ dependence of the RTD, respectively.
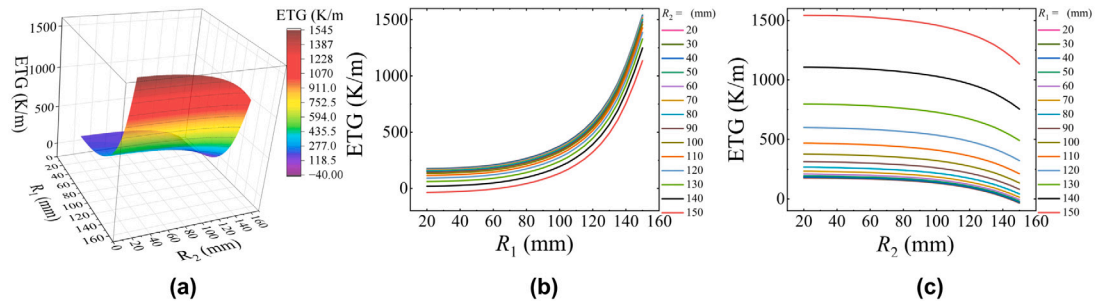


**Fig. 10.** (a) $R_1$ and $R_2$ dependence of the ETG, shown as the 3-D view; (b) $R_1$ dependence of the ETG for different $R_2$; (c) $R_2$ dependence of the ETG for different $R_1$.

due to that the value of the ETG depends on the radial variation of the magnitude of heat released at the edge. It should be noted that, if $L$ or $d$ is too small, the shape of the seed surface radial temperature distribution curve will be concave or too flat, as shown in Fig. 5(f) and Fig. 5(j). To avoid this phenomenon, we set $L \geq 20$ mm and $d \geq 20$ mm in this study.

### 3.2. The varying of $R_1$ and $R_2$

As seen in Fig. 8, the heat flux has been shown, with the parameters $L = 25$ mm; $d = 28$ mm; $P_1 = 1$ kW; $P_2 = 3$ kW, and $P_3 = 23$ kW. Obviously, the heat flux path changes when the length of each insulation separator is adjusted. The insulation separator plays an important role as a switch, by shortening it, the heat in the lower will cruise to the upper from the gap between the crucible and graphite insulation separator. Besides, a part of the thermal radiation path of the heater is also blocked by the insulation separator.

When insulation separators are long enough, as shown in Fig. 8(a) with $R_1 = 150$ mm and $R_2 = 150$ mm, the crucible wall of each part is heated by the thermal radiation of the heater respectively, and then the heat can only be mainly transferred through the crucible wall into the growth cell, to be mostly released through the seed holder at last. Although $R_2$ is quite short in Fig. 8(b), $R_1$ is long enough to close the gap and stop the heat to escape near the upper insulation separator. As a result, the heat can still only be mainly released through the seed holder, same as shown in Fig. 8(a). Besides, the thermal radiation of *heater*2 and *heater*3 can completely arrive the crucible wall. In addition, the heat of the gas around *heater*2 and *heater*3 will get mixed together and then transport upwards because there is no block between them when $R_2$ is quite small. Consequently, the heat transferred through the upper crucible wall to the growth cell enlarges. When $R_1$ is quite
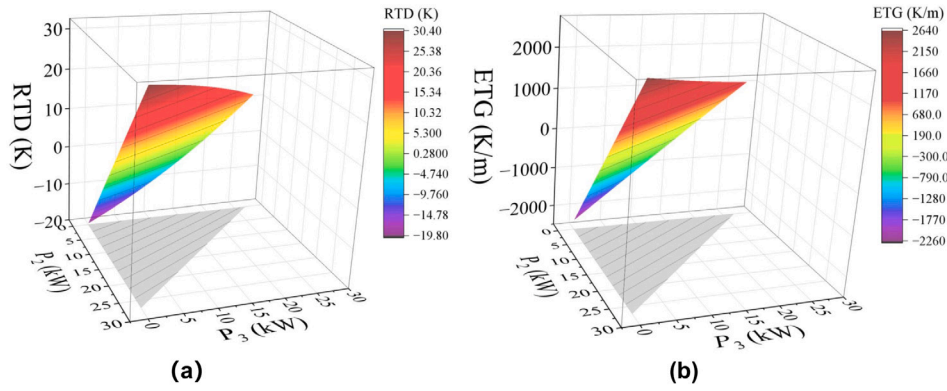
**Fig. 11.** $P_2$ and $P_3$ dependence of (a) the RTD and (b) ETG for $P_{total}$ = 27 kW, shown as the 3-D view.
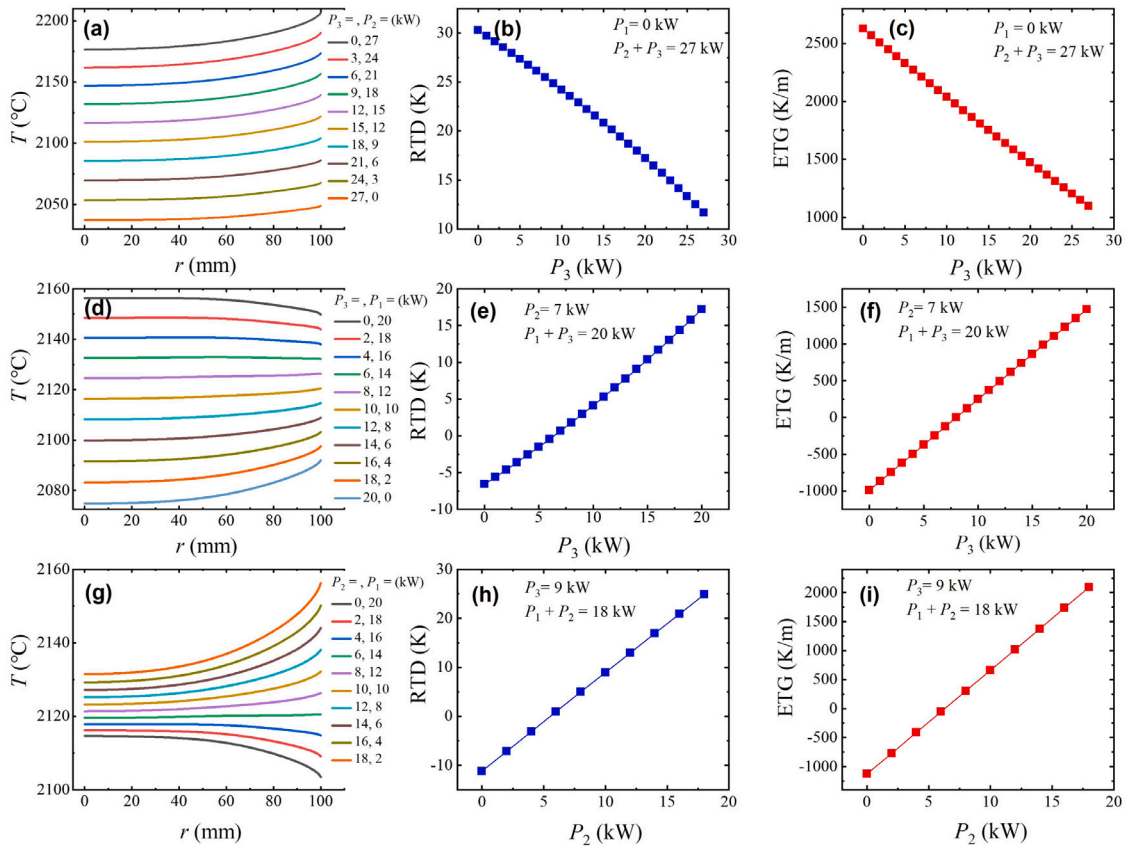


**Fig. 12.** (a) Radial temperature distribution, (b) $P_3$ dependence of the RTD, and (c) ETG, for $P_2 + P_3$ = 27 kW. (d) Radial temperature distribution, (e) $P_3$ dependence of the RTD, and (f) ETG, for $P_1 + P_3$ = 20 kW. (g) Radial temperature distribution, (h) $P_2$ dependence of the RTD, and (i) ETG, for $P_1 + P_2$ = 18 kW.

small, the gap becomes another channel to release the heat, as shown in Fig. 8(c). The heat released through the seed holder reduces markedly because much is transferred outside through the gap between the upper insulation separator and crucible.

Considering the heat flux discussed above, we can easily understand the results in Fig. 9, which displays the $R_1$ and $R_2$ dependence of the RTD. As is shown, with the increase of $R_1$ and $R_2$, the RTD shows two opposite behaviors of increasing and decreasing respectively. Fig. 9(b) and (c) demonstrate the radial temperature distribution on the surface of the seed crystal with $R_1$ = 150 mm and $R_2$ = 150 mm, respectively. It is worth noting that the shapes of the temperature curves change and the curves drop at the edge for small values of $R_1$, as seen in Fig. 9(c), such that the RTD even decrease to negative values. As seen in Fig. 8(a) with $R_1$ = 150 mm and $R_2$ = 150 mm, the heat flux and

the isothermals near the seed crystal in the thermal field are displayed, and a non-negligible amount of heat is transferred into the growth cell through the crucible wall near the seed crystal edge. Obviously, the transferred heat in Fig. 8(b) at the same position enlarges so that the edge temperature will be relatively high, because of the decrease of $R_2$ as discussed before, which explains the behavior in Fig. 9(b). In contrast, the heat in Fig. 8(c) is released outside at the same position, resulting in a drop at the end of the isothermals, which accounts for the behavior in Fig. 9(c).

For the ETG, as shown in Fig. 10, its behavior is similar to that of the RTD, contrary to the role of graphite insulation "Hat". This is due to that the length of insulation separators controls the heat transferred near the seed crystal edge along the radial direction, with which the RTD and ETG behave similarly.
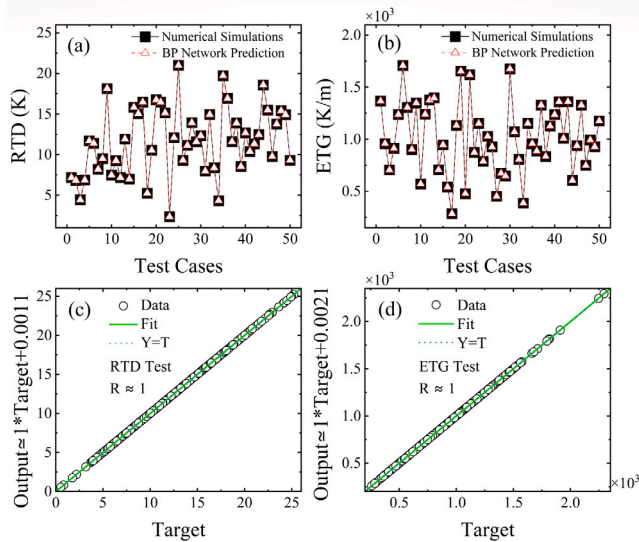
**Fig. 13.** Comparison of the numerical simulation values and BP network predictions for (a) the RTD and ETG; The correlation coefficients between the numerical simulation results and BP network predictions for (c) the RTD and (d) ETG.
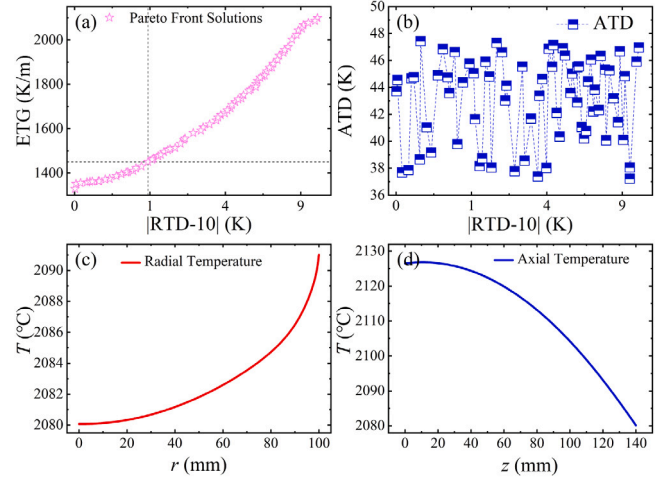


**Fig. 14.** (a) Pareto front solutions for the last generation and the intersection of two perpendicular dotted lines denote the candidate solution we choose; (b) The corresponding ATDs of the Pareto front solutions; (c) The radial temperature distribution on the seed crystal surface of the optimized condition; (d) The central axial temperature distribution (from point $C$ to point $A$ in Fig. 2(a)) of the optimized condition.

### 3.3. The varying of power

Finally, the power distribution of each heater also plays a decisive role in the RTD and ETG. Fig. 11 shows the schematic diagrams of $P_2$ and $P_3$ dependence of the RTD and ETG, with the parameters $L = 25$ mm; $d = 28$ mm; $R_1 = R_2 = 150$ mm. In this study, we set total power $P_{total} = P_1 + P_2 + P_3 = 27$ kW to ensure that the temperature on the seed surface is suitable for SiC crystal growth. It is seen that the RTD and ETG behave similarly with the varying of $P_2$ and $P_3$, both of them increase with the increase of the sum of $P_2$ and $P_3$. And if $P_2 + P_3$ is constant, they decrease with the increase of $P_3$, which is also shown in Fig. 12(a)–(c) with $P_2 + P_3 = 27$ kW. When $P_1 + P_3$ is constant, as shown in Fig. 12(d)–(f) with $P_1 + P_3 = 20$ kW, the RTD and ETG increase with $P_3$ increasing. Moreover, with the increase of $P_1$, the radial temperature curves drop at the edge, such that the RTD and ETG even fall below zero, as seen in Fig. 12(d). When $P_1 + P_2$ is constant, as shown in Fig. 12(g)–(i) with $P_1 + P_2 = 18$ kW, the RTD and ETG increase when $P_2$ increases, and they will also fall below zero when $P_1$ increases.

Thus, it can be concluded that, for the RTD and ETG, $P_2$ (the power of $Heater2$) has the most positive effect, then $P_3$ (the power of $Heater3$); $P_1$ (the power of $Heater1$) has the negative effect. This phenomenon is due to that $Heater2$ directly heats the crucible wall around the SiC seed crystal by thermal radiation and has a greater effect on the heat transferred inside near the seed crystal edge along the radial direction, which accounts for the same behavior of the RTD and ETG. However, $Heater1$ directly heats the seed holder by thermal radiation. When $P_1$ increases, the temperature of the seed holder will be higher than that in the lower area and the heat will be transferred outside through the crucible wall. Therefore, we set $P_2 + P_3 > 20$ kW to ensure that the temperature of the source material is much higher than that of the seed crystal.

### 3.4. BP network training

So far, we have discussed the roles of the graphite insulation "Hat", the length of the graphite insulation separator, and the power distribution play on ETD and RTD. Then, we need to use the BP neural network to map the complex non-linear relationships between the optimizing parameters ($L$, $d$, $R_1$, $R_2$, $P_2$, and $P_3$) and targets (the RTD and ETG).

**Table 1**
Ranges of training parameters.

| Parameter | Lower limit | Upper limit |
|---|---|---|
| $L$ (mm) | 20 | 40 |
| $d$ (mm) | 20 | 50 |
| $R_1$ (mm) | 110 | 150 |
| $R_2$ (mm) | 50 | 150 |
| $P_2$ (kW) | 0 | 27 |
| $P_3$ (kW) | 0 | 27 |

It is well known that the precision of a BP Network model largely depends on the diversity and reservoir of the training data [39], which are obtained from the numerical simulations in this study. Hence, we have collected 2000 datasets of the optimizing parameters and corresponding targets, with the ranges of parameters shown in Table 1. The constructed BP neural network has 2 hidden layers with 15 neurons in each layer, and the Bayesian Regulation back-propagation is used as a training algorithm. The training results of the test cases for the RTD and ETG are shown in Fig. 13, with an average relative error of less than 0.1% and correlation coefficients of 1 for the RTD and ETG, demonstrating that the results are satisfying.

### 3.5. NSGA-II optimization

In this study, the optimal thermal field is set as the RTD closest to 10 K and ETG as large as possible, which is a two-objective optimization problem. In the last step of the optimization, the well-trained BP network coupled with NSGA-II is used to search for the solution that we need. There are 200 candidates in each generation, and the termination criterion is set to 600 iterations. After iterative computation, the candidates are non-dominated sorted by target function values and crowd distance, with the Pareto front solutions for the last generation shown in Fig. 14(a). As shown in Fig. 14(a), the ETGs of the Pareto front solutions are large enough (1300–2000 K/m), and the RTD that meets the requirement of optimal thermal field in this study is set to be no more than 1 K away from 10 K. Hence, we select the candidate that |RTD-10|(K) is the maximum under 1 K to get the ETG as large as possible under the condition of meeting the requirement, as is shown by the intersection of two perpendicular dotted lines in Fig. 14(a), with the parameters $L = 20.2$ mm, $d = 42.5$ mm, $R_1 = 147.6$ mm, $R_2 = 134.8$ mm, $P_1 = 0.1$ kW, $P_2 = 5.2$ kW, and $P_3 = 21.7$ kW. The calculated RTD is 10.9 K and ETG is 1447.7 K/m by the numerical simulation
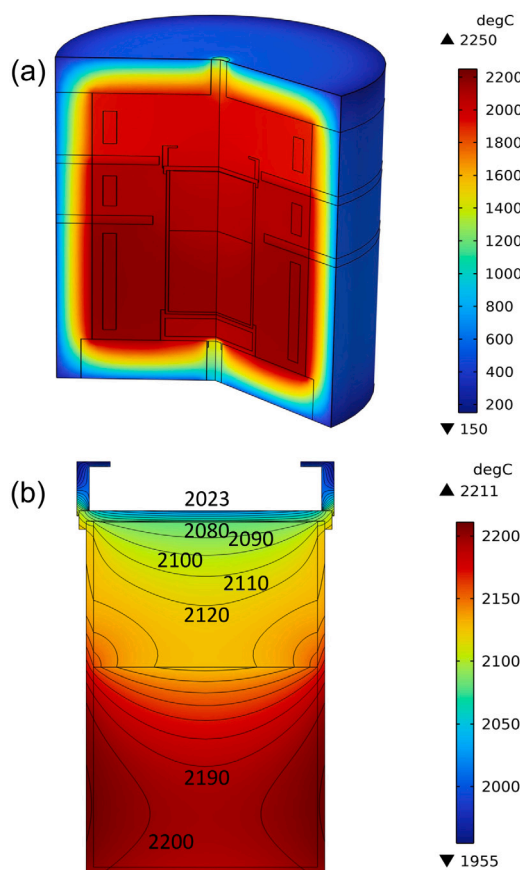
**Fig. 15.** (a) The 3D axis-symmetric thermal field of the furnace with the color scale; (b) The 2D axis-symmetric thermal field of the crucible with the color scale, and the lines denote the isotherms.

distribution results are obtained. In this work, 6 optimizing parameters ($L$, $d$, $R_1$, $R_2$, $P_2$, and $P_3$) and 2 target parameters (the RTD and ETG) that significantly affect the radial temperature distribution on the seed crystal surface are investigated, and the complex non-linear relationship between them is mapped by the BP neural network. Then, the Pareto frontier solutions are obtained by using NSGA-II and the optimal candidate is selected based on the optimal thermal field we set. The optimized condition gives birth to a slightly convex temperature distribution curve on the seed crystal, with an RTD of 10.9 K and ETG of 1447.7 K/m.

**CRediT authorship contribution statement**

**Binjie Xu:** Methodology, Formal analysis, Software, Validation, Formal analysis, Investigation, Data curation, Writing – original draft, Visualization. **Xuefeng Han:** Conceptualization, Resources, Writing – review & editing, Supervision, Project administration. **Suocheng Xu:** Resources. **Deren Yang:** Funding acquisition, Resources. **Xiaodong Pi:** Funding acquisition, Supervision, Writing – review & editing.

**Declaration of competing interest**

The authors declare that they have no known competing financial interests or personal relationships that could have appeared to influence the work reported in this paper.

**Data availability**

Data will be made available on request

**Acknowledgments**

**References**

[1] Xu She, Alex Q. Huang, Óscar Lucía, Burak Ozpineci, Review of silicon carbide power devices and their applications, IEEE Trans. Ind. Electron. 64 (10) (2017) 8193–8205.

[2] Tsunenobu Kimoto, Bulk and epitaxial growth of silicon carbide, Prog. Cryst. Growth Charact. Mater. 62 (2) (2016) 329–351, Special Issue: Recent Progress on Fundamentals and Applications of Crystal Growth; Proceedings of the 16th International Summer School on Crystal Growth (ISSCG-16).

[3] Nick G. Wright, Alton B. Horsfall, Konstantin Vassilevski, Prospects for SiC electronics and sensors, Mater. Today 11 (1) (2008) 16–21.

[4] Yuanchao Huang, Rong Wang, Yixiao Qian, Yiqiang Zhang, Deren Yang, Xiaodong Pi, Theoretical study on the improvement of the doping efficiency of al in 4h-SiC by co-doping group-IVB elements, Chin. Phys. B 31 (4) (2022) 046104.

[5] Im-Gyu Yeo, Woo-Sung Yang, Jong-Hwi Park, Heui-Bum Ryu, Won-Jae Lee, Byoung-Chul Shin, Shigehiro Nishino, Two-inch a-plane (11-20) 6H-SiC crystal grown by using the pvt method from a small rectangular substrate, J. Korean Phys. Soc. 58 (5) (2011) 1541–1544.

[6] Anant Agarwal, Mrinal Das, Sumithra Krishnaswami, John Palmour, James Richmond, Sei-Hyung Ryu, SiC power devices - an overview, MRS Online Proc. Libr. (OPL) 815 (2004) 243–254.

[7] J.A. Lely, Darstellung von einkristallen von siliziumcarbid und beherrschung von art und menge der eingebauten verunreinigungen, Ber. Dtsch. Keram. Ges. 32 (1) (1955) 229.

[8] Yu.M. Tairov, V.F. Tsvetkov, Investigation of growth processes of ingots of silicon carbide single crystals, J. Cryst. Growth 43 (2) (1978) 209–212.

[9] Yu.M. Tairov, V.F. Tsvetkov, General principles of growing large-size single crystals of various silicon carbide polytypes, J. Cryst. Growth 52 (1981) 146–150.

[10] K. Semmelroth, N. Schulze, G. Pensl, Growth of SiC polytypes by the physical vapour transport technique, J. Phys.: Condens. Matter 16 (17) (2004) S1597.

[11] Luo Hao, Zhang Xuqing, Yang Deren, Pi Xiaodong, Research progress on high-purity SiC powder for single crystal SiC growth, J. Synth. Cryst. 50 (8) (2021) 1562–1574.

under these optimal parameter values, which are very close to the predictions by NSGA-II as the RTD is 11.0 K and ETG is 1450.1 K/m. Fig. 14(c) shows the radial temperature distribution curve on the seed crystal surface of the optimized condition, by numerical simulation, which appears a slightly convex shape.

Under the optimized condition, the RTD is low enough (10.9 K) to ensure a slightly convex surface of the crystal. Besides, the large ETG (1447.7 K/m) ensures that the crystal edges are polycrystal-free. Additionally, ATD is also large (46.4 K) enough for the SiC source powder to sublimate upwards, as is shown in Fig. 14(b) and (d). Lastly, the axial temperature gradient inside the source powder, as is seen in Fig. 15(b), also guarantees a positive growth rate in the optimized thermal field. The growth rate in the center of the SiC seed is estimated as 43 μm/h for $P_{argon} = 100$ Pa, according to Eq. (1). However, the condition in our model is much different from that in Eq. (1), the constants $a$, $b$, and $c$ are not clear in our model as a result. Besides, the temperature inside the source powder is much higher than the surface, and therefore the global ATD/$L_z$ of the whole source powder is higher than that just calculated from the surface. Consequently, the growth rate in our model is higher than that estimated from Eq. (1).

**4. Conclusions**

In this paper, we have designed a "3 separation heater method" for SiC crystal growth, and the numerical simulation has been carried out by the FEM. It is found that 3 important parts of the growth cell can be heated independently by 3 heaters, to realize the temperature control separately. By adjusting the structural parameters and the power parameters of the 3 heaters, a series of different temperature

[12] J. Drowart, G. De Maria, Mark G. Inghram, Thermodynamic study of SiC utilizing a mass spectrometer, J. Chem. Phys. 29 (5) (1958) 1015–1021.

[13] Didier Chaussende, Kanaparin Ariyawong, Nikolaos Tsvdaris, Martin Seiss, Yun Ji Shin, Jean Marc Dedulle, Roland Madar, Eirini Sarigiannidou, Joseph La Manna, Odette Chaix-Plucher, Thierry Ouisse, Open issues in SiC bulk growth, in: Silicon Carbide and Related Materials 2013, in: Materials Science Forum, vol. 778, Trans Tech Publications Ltd, 2014, pp. 3–8.

[14] Xi Liu, Bo yuan Chen, Li-Xin Song, Er-Wei Shi, Zhi-Zhan Chen, The behavior of powder sublimation in the long-term pvt growth of SiC crystals, J. Cryst. Growth 312 (9) (2010) 1486–1490.

[15] Z.G. Herro, B.M. Epelbaum, M. Bickermann, P. Masri, A. Winnacker, Effective increase of single-crystalline yield during pvt growth of SiC by tailoring of temperature gradient, J. Cryst. Growth 262 (1) (2004) 105–112.

[16] Aman Arora, Akhilesh Pandey, Ankit Patel, Sandeep Dalal, Brajesh S. Yadav, Anshu Goyal, R. Raman, O.P. Thakur, Renu Tyagi, Polytype switching identification in 4H-SiC single crystal grown by pvt, J. Mater. Sci., Mater. Electron. 31 (19) (2020) 16343–16351.

[17] Shengtao Zhang, Guofeng Fan, Tie Li, Lili Zhao, Optimization of thermal field of 150 mm SiC crystal growth by pvt method, RSC Adv. 12 (2022) 19936–19945.

[18] Mattia Musolino, Xueping Xu, Hui Wang, Varathajan Rengarajan, Ilya Zwieback, Gary Ruland, Danilo Crippa, Marco Mauceri, Michele Calabretta, Angelo Messina, Paving the way toward the world's first 200mm SiC pilot line, Mater. Sci. Semicond. Process. 135 (2021) 106088.

[19] T. Shiramomo, B. Gao, F. Mercier, S. Nishizawa, S. Nakano, Y. Kangawa, K. Kakimoto, Thermodynamical analysis of polytype stability during pvt growth of SiC using 2d nucleation theory, in: The Proceedings of the 18th American Conference on Crystal Growth and Epitaxy, J. Cryst. Growth 352 (1) (2012) 177–180.

[20] Takahiro Nakano, Naoto Shinagawa, Masahiro Yabu, Noboru Ohtani, Formation and multiplication of basal plane dislocations during physical vapor transport growth of 4H-SiC crystals, J. Cryst. Growth 516 (2019) 51–56.

[21] B. Gao, K. Kakimoto, Optimization of power control in the reduction of basal plane dislocations during pvt growth of 4H-SiC single crystals, J. Cryst. Growth 392 (2014) 92–97.

[22] Peter.J. Wellmann, Review of SiC crystal growth technology, Semicond. Sci. Technol. 33 (10) (2018) 103001.

[23] Xiaolin Wang, Dang Cai, Hui Zhang, A novel method to increase the growth rate in sublimation crystal growth of advanced materials, Int. J. Heat Mass Transfer 50 (7) (2007) 1221–1230.

[24] Q.-S. Chen, H. Zhang, R.-H. Ma, V. Prasad, C.M. Balkas, N.K. Yushin, Modeling of transport processes and kinetics of silicon carbide bulk growth, in: Proceedings of the 12th American Conference on Crystal Growth and Epitaxy, J. Cryst. Growth 225 (2) (2001) 299–306.

[25] Optimization of the design of a crucible for a SiC sublimation growth system using a global model, J. Cryst. Growth 310 (7) (2008) 1810–1814.

[26] B. Gao, K. Kakimoto, Dislocation-density-based modeling of the plastic behavior of 4H-SiC single crystals using the alexander-haasen model, J. Cryst. Growth 386 (2014) 215–219.

[27] R.-H. Ma, Q.-S. Chen, H. Zhang, V. Prasad, C.M. Balkas, N.K. Yushin, Modeling of silicon carbide crystal growth by physical vapor transport method, J. Cryst. Growth 211 (1) (2000) 352–359.

[28] B. Gao, X.J. Chen, S. Nakano, S. Nishizawa, K. Kakimoto, Analysis of SiC crystal sublimation growth by fully coupled compressible multi-phase flow simulation, J. Cryst. Growth 312 (22) (2010) 3349–3355.

[29] Hao Luo, Xuefeng Han, Yuanchao Huang, Deren Yang, Xiaodong Pi, Numerical simulation of a novel method for pvt growth of SiC by adding a graphite block, Crystals 11 (12) (2021).

[30] Lu Jiazheng, Zhang Hui, Zheng Lili, Ma Yuan, Song Depeng, Thermal field design and optimization of resistance heated large-size SiC crystal growth system, J. Synth. Cryst. 51 (3) (2022) 371–384.

[31] Shin ichi Nishizawa, Tomohisa Kato, Kazuo Arai, Effect of heat transfer on macroscopic and microscopic crystal quality in silicon carbide sublimation growth, in: Proceedings of the Fifth Workshop on Modeling in Crystal Growth, J. Cryst. Growth 303 (1) (2007) 342–344.

[32] Shengtao Zhang, Guoqing Fu, Hongda Cai, Junzhi Yang, Guofeng Fan, Yanyu Chen, Tie Li, Lili Zhao, Design and optimization of thermal field for pvt method 8-inch SiC crystal growth, Materials 16 (2) (2023).

[33] Peng Tan, Wenyu Kang, Jun Yin, Junyong Kang, 200 Mm silicon carbide bulk growth optimisation: mass transport controlled by a designed gas deflector, Phys. Scr. 97 (10) (2022) 105708.

[34] R. Ma, H. Zhang, V. Prasad, M. Dudley, Growth kinetics and thermal stress in the sublimation growth of silicon carbide, Cryst. Growth Des. 2 (3) (2002) 213–220.

[35] Natasha Dropka, Martin Holena, Optimization of magnetically driven directional solidification of silicon using artificial neural networks and gaussian process models, J. Cryst. Growth 471 (2017) 53–61.

[36] Zhengjie Chen, Wenhui Ma, Kuixian Wei, Jijun Wu, Shaoyuan Li, Keqiang Xie, Guoqiang Lv, Artificial neural network modeling for evaluating the power consumption of silicon production in submerged arc furnaces, Appl. Therm. Eng. 112 (2017) 226–236.

[37] Batta Mahesh, Machine learning algorithms -a review, 2019.

[38] M.I. Jordan, T.M. Mitchell, Machine learning: Trends, perspectives, and prospects, Science 349 (6245) (2015) 255–260.

[39] Xiaofang Qi, Wencheng Ma, Yifan Dang, Wenjia Su, Lijun Liu, Optimization of the melt/crystal interface shape and oxygen concentration during the czochralski silicon crystal growth process using an artificial neural network and a genetic algorithm, J. Cryst. Growth 548 (2020) 125828.

[40] Yifan Dang, Lijun Liu, Zaoyang Li, Optimization of the controlling recipe in quasi-single crystalline silicon growth using artificial neural network and genetic algorithm, J. Cryst. Growth 522 (2019) 195–203.

[41] Kai Zhang, Yulin Lv, A multiobjective rna secondary structure prediction algorithm based on nsgaii, in: 2018 IEEE SmartWorld, Ubiquitous Intelligence & Computing, Advanced & Trusted Computing, Scalable Computing & Communications, Cloud & Big Data Computing, Internet of People and Smart City Innovation (SmartWorld/SCALCOM/UIC/ATC/CBDCom/IOP/SCI), 2018, pp. 1450–1454.

[42] Mohammad Hossein Ahmadi, Mohammad Ali Ahmadi, Multi objective optimization of performance of three-heat-source irreversible refrigerators based algorithm nsgaii, Renew. Sustain. Energy Rev. 60 (2016) 784–794.

[43] Pengfei Han, Bing Gao, Botao Song, Yue Yu, Xia Tang, Botao Liu, Large-sized gan crystal growth analysis in an ammonothermal system based on a well-developed numerical model, Materials 15 (12) (2022).

[44] Feijiang Huang, Junjun Zhang, Qingxiao Shan, Chenglin Cai, Huafu Liu, The research of the plant leaves identification method based on 3-layers bp neutral network, Cluster Comput. 22 (5) (2019) 11143–11152.

[45] D.E. Goldberg, Genetic algorithms in search, optimization and machine learning, in: Applied Mathematics and Computation, Addison-Wesley, Reading, MA, 1989.

[46] Ling Wang, A hybrid genetic algorithm-neural network strategy for simulation optimization, Appl. Math. Comput. 170 (2) (2005) 1329–1343.

[47] Kalyanmoy Deb, Samir Agrawal, Amrit Pratap, T. Meyarivan, A fast elitist non-dominated sorting genetic algorithm for multi-objective optimization: Nsga-ii, in: Marc Schoenauer, Kalyanmoy Deb, Günther Rudolph, Xin Yao, Evelyne Lutton, Juan Julian Merelo, Hans-Paul Schwefel (Eds.), Parallel Problem Solving from Nature PPSN VI, Springer, Berlin, Heidelberg, 2000, pp. 849–858.

[48] K. Deb, A. Pratap, S. Agarwal, T. Meyarivan, A fast and elitist multiobjective genetic algorithm: Nsga-ii, IEEE Trans. Evol. Comput. 6 (2) (2002) 182–197.